Nanoscale

PAPER

Published on 22 May 2026
Licence and permissions

Cite this: *Nanoscale*, 2026, **18**, 13587

Tuning humidity response in 2D MOF membranes through nanosheet geometry

Liangliang Peng,[a,b,d] Zhiqing Lan,[b] Peidong Bao,[a,b,d] Dekai Cai,[a,b,d] Jiangfeng Lu *[b] and Gang Xu [b,c,d]

Received 2nd February 2026,
Accepted 20th May 2026

DOI: 10.1039/d6nr00445h

rsc.li/nanoscale

Variations in the geometry of two-dimensional metal–organic framework (2D MOF) nanosheets provide an effective handle for tuning the humidity response of lamellar membranes. Using layered CuTCPP as a model system, we show that membranes assembled from smaller and thinner nanosheets exhibit up to a 37-fold enhancement in humidity sensitivity compared with those composed of larger and thicker counterparts. Reducing nanosheet thickness and lateral size increases the accessible nanosheet surface within the lamellar architecture and promotes more uniform stacking with confined interlayer voids. These surface-dominated structural features facilitate the formation of continuous, water-mediated charge transport pathways. As a result, the membranes display faster response kinetics, higher steady-state currents, and enhanced low-humidity performance. This work establishes a clear geometry–structure–property relationship and highlights nanosheet surface accessibility as a key factor governing humidity-responsive transport in 2D MOF membranes.

Introduction

Two-dimensional metal–organic frameworks (2D MOFs) are a unique class of lamellar materials.[1–5] To date, strategies for tailoring the functionality of 2D MOFs primarily focus on chemical design, such as ligand modification or metal-node engineering.[6–10] However, despite the significant influence of nanosheet geometry, such as lateral size and thickness, on nanosheet rearrangement, intersheet packing, and transport pathways within macroscopic membranes,[11–15] its role has not been sufficiently explored. Unlike many conventional 2D materials, which typically require post-synthetic processing to adjust interlayer structures,[16–19] 2D MOFs offer a unique opportunity to tune nanosheet geometry directly during synthesis procedures, enabling the isolation of geometry-driven effects on macroscopic properties. Understanding geometry–property relationships is therefore critical for optimizing 2D MOF-based materials.

Humidity sensing provides a sensitive platform to probe such geometry–structure relationships,[20–24] as water molecules readily interact with confined lamellar architectures.[25–28] Consequently, variations in nanosheet geometry can induce measurable differences in membrane stacking and intersheet organization, resulting in distinct humidity-dependent electrical responses.[23,29,30] Despite this intuitive connection, systematic experimental studies that directly correlate nanosheet geometry with membrane architecture and humidity response remain scarce in 2D MOFs.

Here, we employ the layered porphyrin MOF CuTCPP (TCPP = 5,10,15,20-tetrakis(4-carboxyphenyl)porphyrin) as a model system to investigate how nanosheet geometry affects membrane architecture and humidity-dependent electrical behavior.[31–35] By controlling the synthesis conditions, CuTCPP nanosheets with distinct lateral sizes and thicknesses were obtained and assembled into highly oriented, flexible membranes. Reducing nanosheet size and thickness alters lamellar stacking, intersheet packing, and connectivity, which in turn modulates water accessibility and charge transport. Membranes composed of smaller and thinner nanosheets show enhanced humidity response, faster kinetics, and improved low-humidity sensitivity, establishing a direct correlation between nanosheet geometry, membrane structure, and sensing performance.

Experimental

Materials

Copper(II) nitrate trihydrate (99%) was purchased from Beijing InnoChem Science & Technology Co., Ltd. Tetrakis(4-carboxy-

[a]*College of Chemistry and Materials Science, Fujian Normal University, Fuzhou, Fujian 350007, P. R. China*
[b]*State Key Laboratory of Structural Chemistry, and Fujian Provincial Key Laboratory of Materials and Techniques toward Hydrogen Energy, Fujian Institute of Research on the Structure of Matter, Chinese Academy of Sciences, Fuzhou, Fujian 350002, P. R. China. E-mail: lujiangfeng@fjirsm.ac.cn*
[c]*University of Chinese Academy of Science (UCAS), Beijing 100049, P. R. China*
[d]*Fujian College, University of Chinese Academy of Sciences, Fuzhou, Fujian 350002, P. R. China*

phenyl)porphyrin ((H$_4$TCPP), 96%+) was purchased from Adamas-Beta. *N*,*N*-Dimethylformamide (DMF, AR) and ethanol (EtOH, AR) were purchased from Sinopharm Chemical Reagent Co., Ltd. All solvents and reagents obtained from commercial sources were used without further purification. Water was deionized before use.

Characterization methods

Powder X-ray diffraction (PXRD) analysis was performed using a Rigaku Smart-Lab X-ray diffractometer with Cu Kα radiation (λ = 0.15418 nm) in the 2θ range from 3° to 50° with a 0.02° step and a step time of 1 s. In-plane and out-of-plane XRD scans were measured using a Rigaku Smart-Lab X-ray diffractometer with Cu Kα radiation (λ = 0.15418 nm) in the 2θ range from 3 to 50° at a scanning rate of 0.5° min^{-1}. Fourier-transform infrared (FTIR) spectra were obtained using a Bruker VERTEX 70 spectrometer. Scanning electron microscopy (SEM) images were obtained using a ZEISS Sigma 500 instrument. Atomic force microscopy (AFM) images were acquired using a Bruker Dimension ICON instrument. Water-vapor adsorption measurements were performed using a MEMS-based thermogravimetric analyzer (LoC-TGA-1002, High-End MEMS Technology Co., Ltd).

Synthesis of CuTCPP nanosheets

CuTCPP nanosheets were synthesized *via* a solvothermal reaction between Cu(NO$_3$)$_2$·3H$_2$O and H$_4$TCPP (5,10,15,20-tetrakis (4-carboxyphenyl)porphyrin) in *N*,*N*-dimethylformamide (DMF).[33–35] Typically, H$_4$TCPP (7.9 mg, 0.01 mmol) and Cu(NO$_3$)$_2$·3H$_2$O (7.3 mg, 0.03 mmol) were dissolved in different volumes of DMF: 6 mL for NS1, 12 mL for NS2, and 18 mL for NS3. The mixtures were sonicated for 5 min at room temperature to ensure complete dispersion. The mixtures were then heated to 35 °C within 1 h and maintained for 10 h, followed by heating to 85 °C over 10 h and further reaction at 85 °C for 24 h. After cooling naturally to room temperature at 5 °C h^{-1}, the purple products were collected by centrifugation and washed with ethanol four times to remove residual reactants and solvents. The purified CuTCPP nanosheets were denoted as NS1, NS2, and NS3.

Preparation of CuTCPP free-standing membranes (M1–M3)

CuTCPP free-standing membranes were fabricated from the as-synthesized CuTCPP nanosheets (NS1–NS3) using a previously reported vacuum-assisted filtration method.[33–36] The membranes derived from NS1, NS2, and NS3 were denoted as M1, M2, and M3, respectively. Typically, 20 mg of CuTCPP nanosheets was dispersed in 200 mL of ethanol in a 300 mL round-bottom flask. The suspension was sealed and sonicated for 15 min to promote uniform dispersion. AFM analysis of nanosheets collected after sonication confirmed that the mild exfoliation process did not significantly alter their original thickness distribution (Fig. S1). For membrane assembly, 20 mL of the CuTCPP nanosheet suspension (0.1 mg mL^{-1}) was vacuum-filtered through a polyvinylidene difluoride (PVDF) membrane filter (pore size: ~0.1 μm; porosity: ~80%; diameter: 25 mm). The collected membranes were dried at 50 °C for 4 h. The resulting membranes exhibited an average thickness of approximately 20 μm and could be readily peeled off from the PVDF substrate.

Results and discussion

Three CuTCPP nanosheet samples (NS1, NS2, and NS3) were synthesized *via* a solvothermal reaction of Cu(NO$_3$)$_2$·3H$_2$O and the TCPP ligand in *N*,*N*-dimethylformamide (DMF), with solvent volumes of 6, 12, and 18 mL, respectively. In the *ab*-plane, CuTCPP forms a porous 2D network in which Cu-metallated porphyrin ligands coordinate to binuclear Cu$_2$(COO)$_4$ paddle-wheel clusters. Each cluster comprises two Cu^{2+} ions bridged by four carboxylate groups from neighboring ligands, linking repeatedly along the plane to form an extended 2D framework (Fig. 1a). Layers stack along the *c*-axis *via* van der Waals interactions (Fig. 1b), adopting AB stacking with each layer laterally shifted by roughly one-quarter of the unit cell along the *a*-axis (Fig. 1c). This lamellar arrangement provides periodic interlayer voids and abundant hydrophilic carboxylate sites. FTIR spectra confirm the nanosheet structure, showing diminished carboxyl stretching vibrations (~1700 and ~1260 cm^{-1}) and disappearance of the C–N stretching band near 966 cm^{-1} after Cu insertion into the porphyrin center (Fig. 1d). XRD patterns agree well with the simulated data, corroborating the expected crystal structure (Fig. 1e).

By adjusting the precursor concentration during the solvothermal reaction, the resultant nanosheets show systematic variations in lateral size and thickness (Fig. 2a–f). SEM images reveal a gradual decrease in lateral size. NS1 forms large, well-defined structures with lateral dimensions around 2–3 μm. Similar to NS1, NS2 also displays a regular nanosheet morphology, with lateral dimensions of approximately 1–2 μm. In contrast, NS3 shows poorly defined sheet boundaries, which can be attributed to its ultrathin nature, making the sheet edges nearly indistinguishable. AFM measurements confirm thicknesses of approximately 100, 60, and 4 nm for NS1, NS2, and NS3, respectively. The nanosheet morphology observed by AFM is consistent with the SEM results.

Free-standing CuTCPP membranes were fabricated by vacuum-assisted filtration of nanosheets dispersed in ethanol.[29–31] Membranes assembled from NS1, NS2, and NS3 were denoted as M1, M2, and M3, respectively. All membranes were mechanically robust, uniform, and laterally continuous (Fig. 3a–c), and could be easily detached to yield free-standing membranes. The membrane thicknesses, measured using a micrometer, were 20, 17, and 11 μm for M1, M2, and M3, respectively (Table S1). Notably, all membranes were fabricated using the same mass of nanosheets; therefore, the differences in thickness originated from variations in nanosheet size and thickness, which led to distinct stacking modes and intersheet void characteristics rather than differences in material loading.

Top-view SEM images (Fig. S2) reveal distinct membrane morphologies. M1 is composed of large, flat nanosheets with

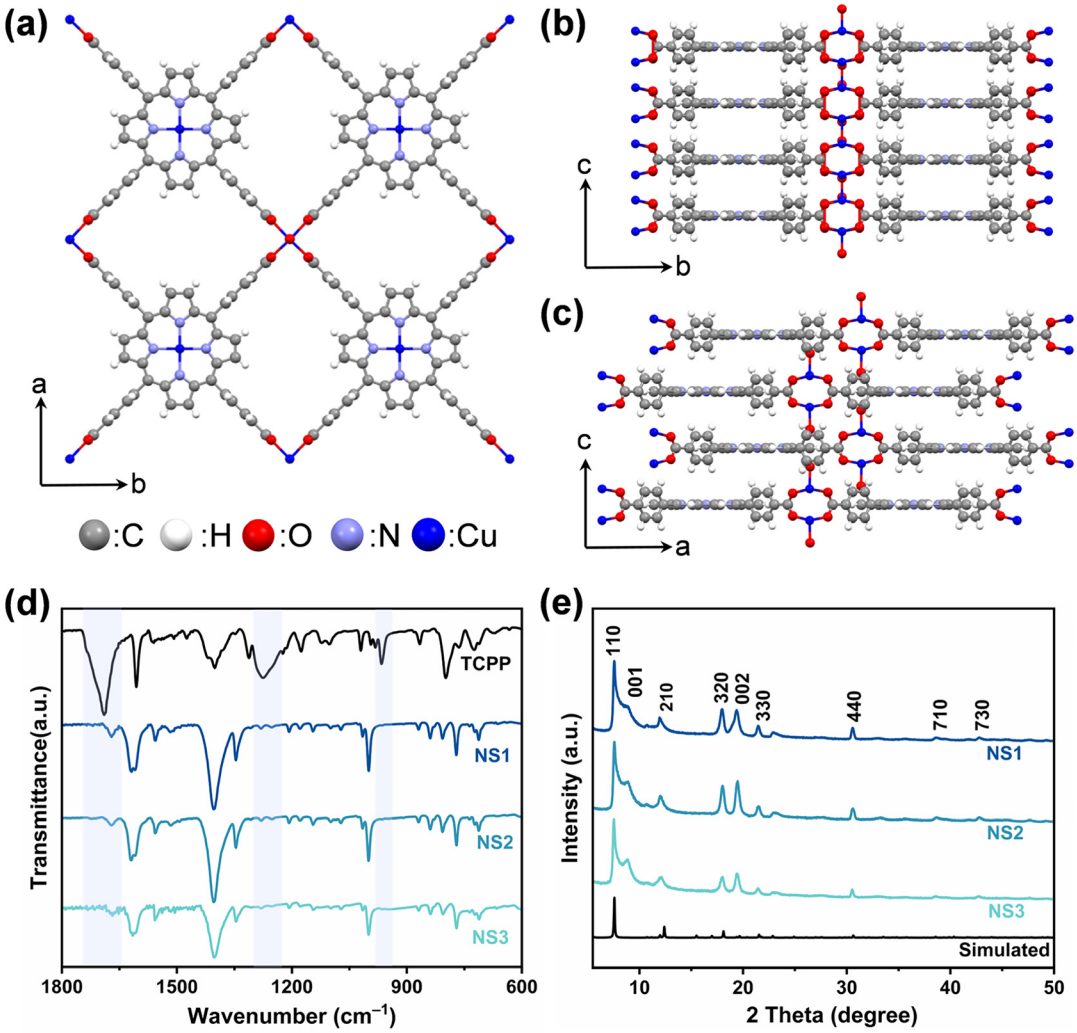

Fig. 1 Structural characterization of CuTCPP nanosheets (NS1–NS3). Simulated crystal structures projected along the *ab*-plane (a), *bc*-plane (b), and *ac*-plane (c). FTIR spectra of the TCPP ligand and CuTCPP nanosheets (d). Powder XRD patterns of CuTCPP nanosheets synthesized under different reagent concentrations (e).

clear boundaries, M2 consists of smaller nanosheets with a smoother surface morphology, and M3 shows a highly continuous surface in which individual nanosheet boundaries are nearly indistinguishable. Cross-sectional SEM images (Fig. 3d–f) show that lamellar stacking was strongly influenced by nanosheet geometry. M1 exhibits loose, wavy stacking with pronounced gaps; M2 shows more regular parallel stacking with minor misalignment; and M3 forms highly aligned, closely packed layers. The corresponding densities were 0.515, 0.773, and 1.029 g cm^{-3} for M1, M2, and M3 (see Table S1 for details), suggesting that smaller and thinner nanosheets promote more efficient and ordered packing.

The XRD results confirm the lamellar structure of the membranes. In-plane patterns (Fig. 3g) show only (*hk*0) reflections, indicating preserved lateral crystallinity, whereas out-of-plane patterns (Fig. 3h) display a dominant (002) reflection, consistent with the preferential alignment of the nanosheets along the *c*-axis. In the powder PXRD pattern, the (001) reflection is prominent because the randomly oriented crystallites contribute equally to all crystallographic planes. In contrast, in the free-standing membranes, the nanosheets adopt a highly oriented lamellar arrangement, which suppresses the (001) reflection and enhances the higher-order (002) reflection in the out-of-plane geometry. The full width at half maximum (FWHM) of the (002) peak increases from M1 to M3, reflecting reduced long-range stacking coherence caused by the faster assembly of thinner nanosheets. In addition, the weaker (150) and (160) reflections in M3 indicate fewer misoriented domains, consistent with the highly aligned stacking observed in the cross-sectional SEM images.

Mechanical testing reveals that flexibility increases from M1 to M3 (Fig. S3). For bending measurements, a separate set of membranes with comparable thicknesses (~10–13 μm) was prepared to exclude thickness-dependent effects. M3 sustains bending to a curvature radius below 0.15 mm (Fig. S4), whereas M1 and M2 show larger minimum bending radii. This

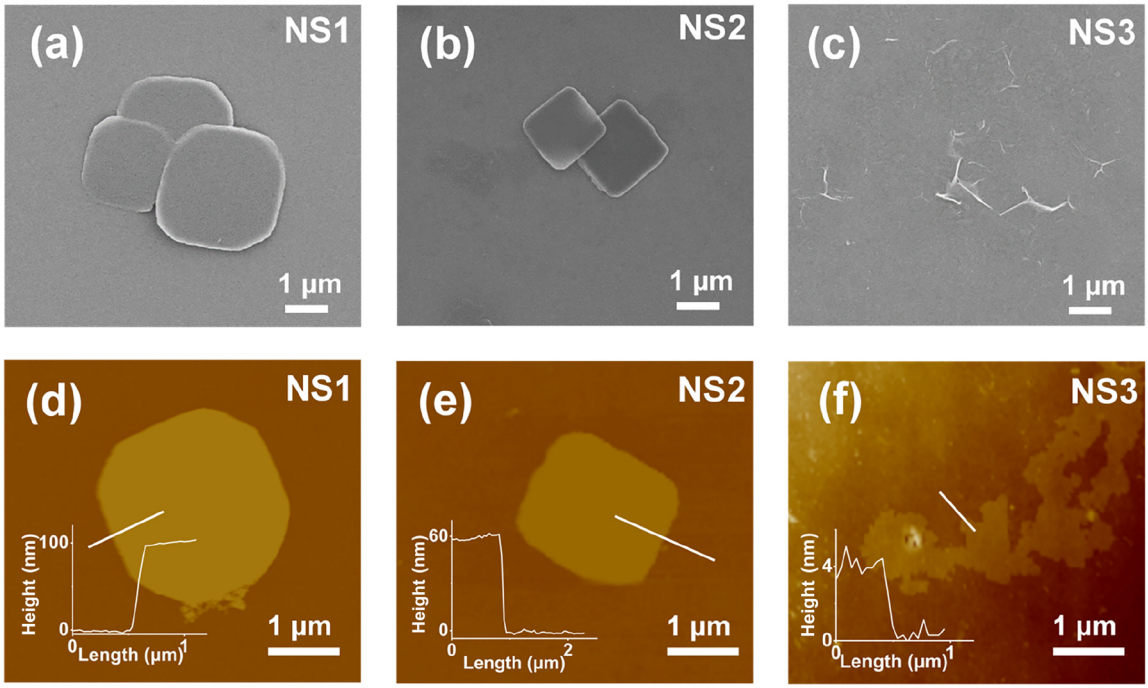

Fig. 2 Morphology and thickness of CuTCPP nanosheets (NS1–NS3). SEM images of NS1, NS2, and NS3 (a–c). AFM height profiles of NS1, NS2, and NS3 (d–f), revealing average thicknesses of approximately 100, 60, and 4 nm, respectively.

improved flexibility can be attributed to the smaller lateral size and reduced thickness of the constituent nanosheets, which create more interfacial slip sites within the lamellar structure and thereby facilitate stress dissipation during deformation. XRD patterns collected after repeated bending (Fig. S5) remain unchanged, confirming the preservation of the lamellar architecture. The mechanical properties are relevant because humidity-responsive lamellar membranes are promising candidates for flexible sensing devices, where structural integrity and continuous charge-transport pathways must be maintained under repeated mechanical deformation.

Beyond differences in thickness and density, the membranes exhibit distinct intersheet void structures. In M1, large and rigid nanosheets stack loosely, forming pronounced mesoscale gaps that limit water-mediated charge transport between adjacent layers. In contrast, the ultrathin nanosheets in M3 assemble into densely packed lamellar layers with nanoscale confined gaps that favor the formation of continuous hydrogen-bonding networks. These structural differences indicate that nanosheet geometry controls the intersheet void environment and therefore plays a critical role in determining the humidity-sensing performance of the membranes.

The humidity-sensing performance of CuTCPP membranes was evaluated by monitoring the DC current under a constant bias. The dominant conduction mechanism shifts with humidity. Under dry conditions, charge transport mainly arises from intrinsic electronic conduction through the π-stacked CuTCPP layers. As humidity increases, adsorbed water molecules bridge adjacent nanosheet surfaces and form hydrogen-bonded pathways, introducing an additional water-mediated transport channel at high relative humidity (RH). Because the applied bias was limited to 1.0 V, the current increase cannot be attributed to Cu-centered redox reactions or water electrolysis. Instead, the adsorbed water molecules act only as transport mediators. A strong dependence on nanosheet geometry is observed across the entire RH range (Fig. 4a). At 5% RH, the steady-state response ($\Delta I/I_0$) increases from M1 (8.3%) to M2 (72.9%) and M3 (117%), indicating that smaller and thinner nanosheets facilitate early water adsorption and charge transport. At 98% RH, M3 exhibits a response of 96 636, nearly 37 times higher than that of M1 (2629) and substantially higher than that of M2 (16 842). Although the three membranes show similar humidity-dependent response profiles, tuning nanosheet geometry produces a substantial improvement in sensitivity and extends the detectable humidity range.

Dynamic response measurements further illustrate the geometry-dependent transport kinetics. Upon a stepwise increase in RH, the response of M3 ($\Delta I/I_0$) rises from 1.14 at 2% RH to 96 636 at 98% RH (Fig. 4b), with a response time of 180 s and a recovery time of 12 s at 98% RH. In contrast, M1 shows a slower response time of 249 s, whereas the recovery times remain similar among the three membranes (detailed in Fig. S7–S10), indicating that adsorption kinetics are strongly influenced by membrane geometry while desorption is mainly governed by the local chemical environment. Repeated humidity cycling at ~98% RH produces stable and reversible current signals (Fig. 4c). The membrane also retained nearly identical responses after repeated cycling and showed negligible performance loss after storage under ambient conditions for 150 days (Fig. S11), confirming excellent operational stability.

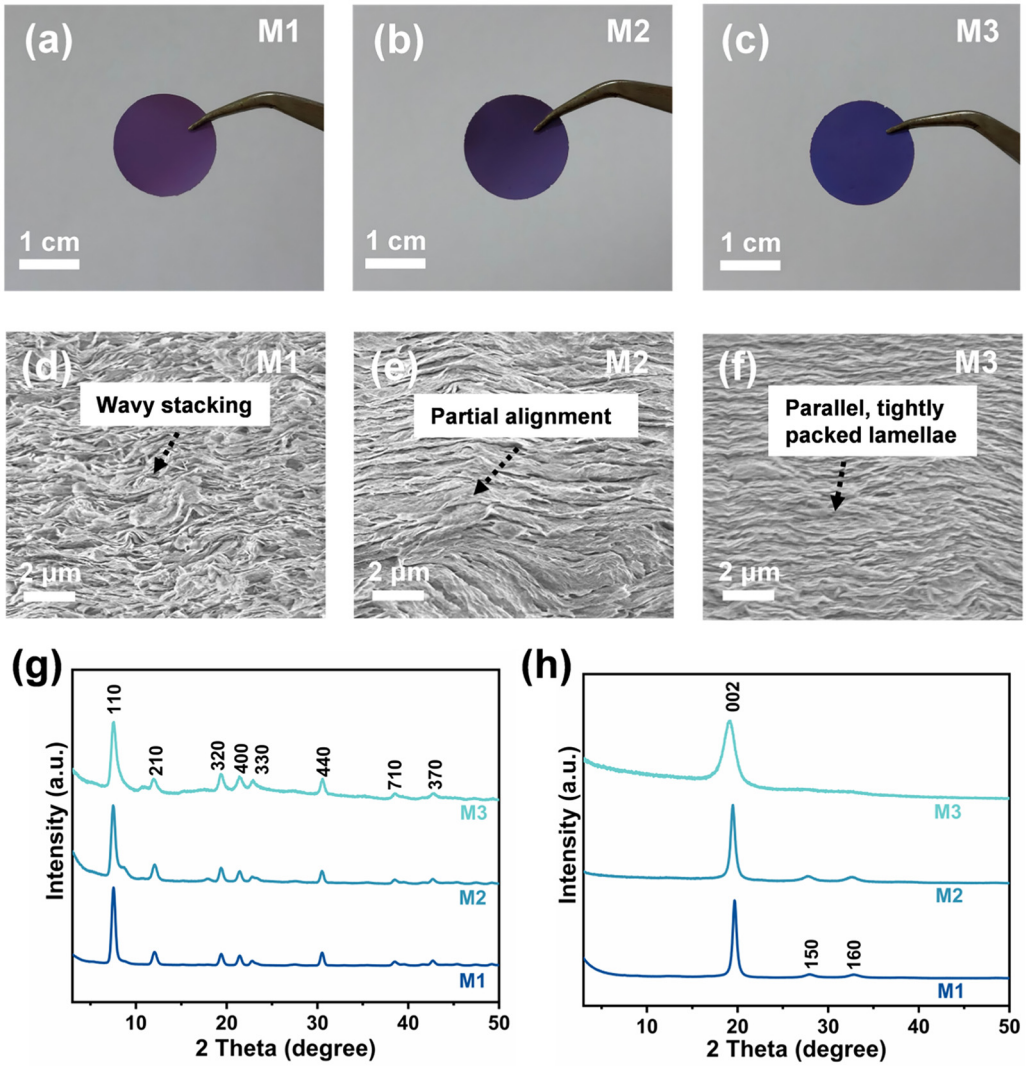

Fig. 3 Structural characterization of CuTCPP membranes (M1–M3). Photographs of CuTCPP free-standing membranes (M1–M3) (a–c). Cross-sectional SEM images of the corresponding membranes (d–f). In-plane X-ray diffraction (XRD) patterns of the three membranes (g). Out-of-plane XRD patterns of the three membranes (h).

Water-vapor adsorption measurements of the nanosheets used for membrane assembly show that the adsorption capacity increases from NS1 to NS3 (Fig. S12), indicating that smaller and thinner nanosheets provide more accessible adsorption sites. In the assembled membranes, previous studies have shown that water adsorption in layered CuTCPP mainly occurs on the nanosheet surfaces.[32] In this work, these surface-confined water molecules bridge adjacent nanosheets and establish hydrogen-bonded pathways across the lamellar structure. Because the more ordered stacking in M3 results in shorter intersheet distances and improved pathway continuity, charge transport becomes significantly more efficient than in the loosely packed M1 membrane. *In situ* FTIR spectra collected under increasing humidity (Fig. S13) show a progressive growth of the O–H stretching and H–O–H bending bands, indicating the accumulation of adsorbed water and the formation of hydrogen-bonded networks within the membrane. Notably, the evolution of these features correlates closely with the conductivity enhancement. To gain molecular-level insight, density functional theory (DFT) calculations were performed (Fig. S14 and S15). The optimized structures reveal that adsorbed water molecules form hydrogen bonds with the carboxylate oxygen atoms of the framework as well as with coordinated water species, generating interconnected hydrogen-bonding networks between adjacent nanosheets. Bader charge analysis indicates partial electron transfer (0.0116 e^{-1}) from the adsorbed water molecules to the framework, which is further supported by differential charge density maps showing electron depletion around the water molecules and accumulation in the Cu–carboxylate coordination region. These results indicate that adsorbed water plays a dual role: it constructs hydrogen-bonded transport pathways and simultaneously modulates the local electronic environment by increasing the charge carrier density. Together, this synergistic effect between

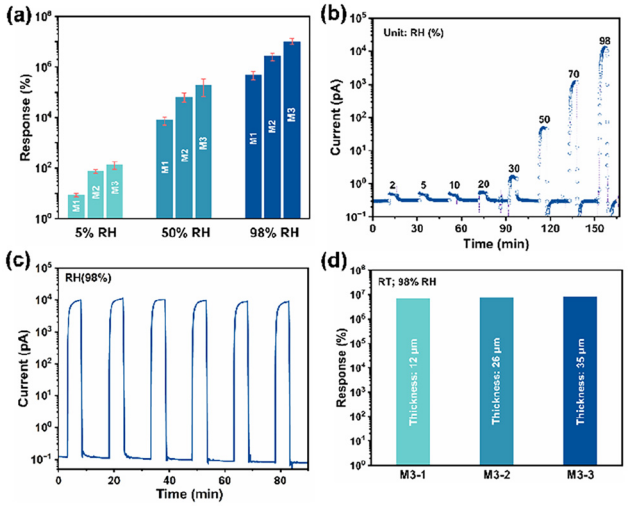

Fig. 4 Humidity-sensing performance of CuTCPP membranes. Steady-state humidity response ($\Delta I/I_0$) of M1, M2, and M3 membranes measured at different relative humidity (RH) levels (a). Dynamic electrical response of the M3 membrane under stepwise RH changes (b). Cyclic electrical response of the M3 membrane at 98% RH (c). Thickness-dependent humidity response of M3 membranes with thicknesses of 12, 26, and 35 μm (d).

the MOF and surface-adsorbed water governs the humidity-activated charge transport in the membranes.

Thickness-dependent measurements of M3 membranes with thicknesses ranging from 12 to 35 μm (Fig. 4d) show negligible variation in the normalized humidity response. Because all membranes were assembled from identical NS3 nanosheets, the local lamellar structure and intersheet water-transport pathways remain essentially unchanged as the membrane becomes thicker. Although the absolute baseline current increases slightly with thickness because of the larger conductive cross-section, the humidity-induced current increases proportionally, resulting in an almost constant $\Delta I/I_0$. This thickness-independent response indicates that the sensing performance is governed primarily by the local nanosheet packing environment rather than the overall membrane thickness. Collectively, these results demonstrate that nanosheet geometry controls water adsorption, lamellar stacking, and interlayer connectivity, which together determine the humidity-sensing performance. Compared with previously reported MOF- and graphene-based humidity sensors, the M3 membrane exhibits a markedly higher response magnitude, particularly under high humidity conditions, highlighting nanosheet geometry regulation as an effective strategy for enhancing sensor sensitivity (Table S2).

Conclusions

In summary, the lateral size and thickness of CuTCPP nanosheets are identified as key parameters governing the humidity-dependent electrical behavior of assembled membranes. Smaller and thinner nanosheets enable more uniform lamellar stacking, reduced intersheet spacing, and increased accessible surface area for water adsorption. These structural features promote the formation of continuous hydrogen-bonded networks across adjacent nanosheets. Combined experimental and theoretical analyses reveal that adsorbed water plays a dual role: it not only constructs hydrogen-bonded transport pathways, but also modulates the local electronic environment through charge redistribution, thereby increasing charge carrier density and facilitating charge transport. As a result, membranes assembled from such nanosheets exhibit significantly enhanced sensing performance, including markedly higher steady-state responses and improved sensitivity at low humidity. Importantly, these improvements arise primarily from nanosheet geometry-induced structural and electronic effects, rather than from chemical modification or membrane thickness. This work establishes a clear geometry–structure–transport relationship and highlights nanosheet geometry as an effective design parameter for tuning the functional behavior of layered 2D MOF membranes, providing useful guidance for the development of high-performance humidity sensing materials.

Author contributions

L. P., J. L. and G. X. conceived the idea. L. P. and J. L. designed the experiments and collected and analysed the data. Z. L., P. B. and D. C. assisted with the experiments and characterization. L. P. and J. L. wrote the manuscript. All authors discussed the results and commented on the manuscript.

Conflicts of interest

There are no conflicts to declare.

Data availability

The data supporting this article have been included as part of the supplementary information (SI). Supplementary information: Fig. S1–S15 and Tables S1 and S2. See DOI: https://doi.org/10.1039/d6nr00445h.

Acknowledgements

This work was financially supported by the National Natural Science Foundation of China (grant no. 22405274, 22325109, 62227815, and 22494633), the Self-deployment Project Research Program of Haixi Institutes, Chinese Academy of Sciences (grant no. CXZX-2023-GS03), and the Key Research Project of the Chinese Academy of Sciences (grant no. KGFZD-145-25-21).

References

1 G. Chakraborty, I. H. Park, R. Medishetty and J. J. Vittal, *Chem. Rev.*, 2021, **121**, 3751–3891.
2 M. Zhao, Y. Huang, Y. Peng, Z. Huang, Q. Ma and H. Zhang, *Chem. Soc. Rev.*, 2018, **47**, 6267–6295.
3 K. A. Adegoke, O. R. Adegoke, R. A. Adigun, N. W. Maxakato and O. S. Bello, *Coord. Chem. Rev.*, 2022, **473**, 214817.
4 M. Zhao, Y. Wang, Q. Ma, Y. Huang, X. Zhang, J. Ping, Z. Zhang, Q. Lu, Y. Yu, H. Xu, Y. Zhao and H. Zhang, *Adv. Mater.*, 2015, **27**, 7372–7378.
5 W. Tang, Y. Cheng, J. Zhu, Y. Zhou, M. Xu and Z. Gu, *Angew. Chem., Int. Ed.*, 2024, e202409588.
6 W. Liu, R. Yin, X. Xu, L. Zhang, W. Shi and X. Cao, *Adv. Sci.*, 2019, **6**, 1802373.
7 J. Park, J. Lim and H. R. Moon, *Trends Chem.*, 2025, **7**, 590–602.
8 S. Mandal, S. Natarajan, P. Mani and A. Pankajakshan, *Adv. Funct. Mater.*, 2021, **31**, 2006291.
9 R. Du, Y. Wu, Y. Yang, T. Zhai, T. Zhou, Q. Shang, L. Zhu, C. Shang and Z. Guo, *Adv. Energy Mater.*, 2021, **11**, 2100154.
10 J. Han, Y. Hao, M. Luo, Z. Xie and Z. Zhou, *Mater. Horiz.*, 2025, **12**, 8334–8350.
11 M. D. P. Bernicola, M. Madrid-Gimeno, N. Murillo-Cremaes, T. Battisti, N. Lozano, K. Kostarelos, J. A. Garrido and E. Del Corro, *Diamond Relat. Mater.*, 2024, **150**, 111722.
12 J. Neilson, E. Caffrey, O. Cassidy, C. Gabbett, K. Synnatschke, E. Schneider, J. M. Munuera, T. Carey, M. Rimmer, Z. Sofer, J. Maultzsch, S. J. Haigh and J. N. Coleman, *ACS Nano*, 2024, **18**, 32589–32601.
13 X. Yu, Y. Cai, T. Wang and T. Yu, *FlatChem*, 2025, **49**, 100774.
14 F. Wang, Z. Zhang, I. Shakir, C. Yu and Y. Xu, *Adv. Sci.*, 2022, **9**, 2103814.
15 H. Ma, X. Jin, Y. Z. Du, L. Y. Dong, X. Hu, W.-C. Li, D. Wang, R. Joshi, G. P. Hao and A. H. Lu, *Chem. Commun.*, 2022, **58**, 5626–5629.
16 R. R. Nair, H. A. Wu, P. N. Jayaram, I. V. Grigorieva and A. K. Geim, *Science*, 2012, **335**, 442–444.
17 R. Krishnamoorthi, F. S. Butt, N. A. Mazlan, S. Chen, N. Radacsi, S. Yang, Y. Yoon and Y. Huang, *J. Membr. Sci.*, 2024, **706**, 122942.
18 D. Yu, L. Sun, Y. Zhang, Y. Song, C. Jia, Y. Wang, Y. Wang, M. J. Kipper, J. Tang and L. Huang, *Chem. Eng. J.*, 2024, **480**, 148009.
19 F. A. Anwar, W. Rahmah and G. T. M. Kadja, *Nano Trends*, 2025, **12**, 100154.
20 C. Cheng, G. Jiang, C. J. Garvey, Y. Wang, G. P. Simon, J. Z. Liu and D. Li, *Sci. Adv.*, 2016, **2**, e1501272.
21 X. Wang, C. Chi, K. Zhang, Y. Qian, K. M. Gupta, Z. Kang, J. Jiang and D. Zhao, *Nat. Commun.*, 2017, **8**, 14460.
22 M. He, Y. Chen, W. Lu, L. Guo, K. Hu, X. Han, I. Vitorica-Yrezabal, C. Dejoie, A. N. Fitch, M. Schröder and S. Yang, *ACS Appl. Mater. Interfaces*, 2024, **16**, 32524–32532.
23 C. D. Williams, P. Carbone and F. R. Siperstein, *ACS Nano*, 2019, **13**, 2995–3004.
24 H. Chen, H. Ma and C. Li, *ACS Nano*, 2021, **15**, 15502–15537.
25 Y. Xu, T. Watermann, H. H. Limbach, T. Gutmann, D. Sebastiani and G. Buntkowsky, *Phys. Chem. Chem. Phys.*, 2014, **16**, 9327–9336.
26 J. B. Mietner, F. J. Brieler, Y. J. Lee and M. Fröba, *Angew. Chem., Int. Ed.*, 2017, **56**, 12348–12351.
27 A. W. Knight, N. G. Kalugin, E. Coker and A. G. Ilgen, *Sci. Rep.*, 2019, **9**, 8246.
28 X. Liu, X. Pan, S. Zhang, X. Han and X. Bao, *Langmuir*, 2014, **30**, 8036–8045.
29 B. Lian, S. De Luca, Y. You, S. Alwarappan, M. Yoshimura, V. Sahajwalla, S. C. Smith, G. Leslie and R. K. Joshi, *Chem. Sci.*, 2018, **9**, 5106–5111.
30 A. Iakunkov and A. V. Talyzin, *Nanoscale*, 2020, **12**, 21060–21093.
31 G. Xu, T. Yamada, K. Otsubo, S. Sakaida and H. Kitagawa, *J. Am. Chem. Soc.*, 2012, **134**, 16524–16527.
32 G. Xu, K. Otsubo, T. Yamada, S. Sakaida and H. Kitagawa, *J. Am. Chem. Soc.*, 2013, **135**, 7438–7441.
33 J. Lu, *Novel Proton Conducting in Free-Standing Coordination Polymer Membranes*, Springer Nature Singapore, Singapore, 2024.
34 J. Lu, Y. Yoshida, M. Maesato and H. Kitagawa, *Angew. Chem., Int. Ed.*, 2022, **61**, e202213077.
35 M. Tian, F. Pei, M. Yao, Z. Fu, L. Lin, G. Wu, G. Xu, H. Kitagawa and X. Fang, *Energy Storage Mater.*, 2019, **21**, 14–21.
36 J. Lu, Y. Yoshida, K. Kanamori and H. Kitagawa, *Angew. Chem., Int. Ed.*, 2023, **62**, e202306942.